Physica Scripta

PAPER

A functionality-switchable device based on coherent perfect absorption with narrowband absorbing performance and sensing function

RECEIVED
10 April 2022

REVISED
14 December 2022

ACCEPTED FOR PUBLICATION
26 January 2023

PUBLISHED
6 February 2023

Yang Zhang[1], **Dan Zhang**[2] **and Haifeng Zhang**[3,*]

[1] College of Integrated Circuit Science and Engineering, Nanjing University of Posts and Telecommunications, Nanjing 210023, People's Republic of China
[2] College of Information Science and Technology, Nanjing Forestry University, Nanjing 210023, People's Republic of China
[3] College of Electronic and Optical Engineering & College of Flexible Electronics (Future Technology), Nanjing University of Posts and Telecommunications, Nanjing 210023, People's Republic of China
[*] Author to whom any correspondence should be addressed.

E-mail: hanlor@163.com

Keywords: switchable dual-function, coherent perfect absorption, narrowband absorber, refractive index sensing

Abstract

An optical structure containing the ferrite defects and Fabry-Pérot cavity with a narrowband absorption feature and a sensing performance is proposed and modeled in theoretical scope. These two features appear alternately on adjacent frequency ranges with modulation of the coherent perfect absorption by altering the phase difference between the two coherent incident lights. For the absorption band, the relative bandwidth reaches 9.7%. Benefiting from the modulation of the magnetic field applied in the ferrite layers, the quality value of the absorption peak is 494.85, which indicates the potential for use as a sensor. There are highly linear relationships between the refractive index values of dielectric layers and the spike absorption frequencies. The accurate analysis of the RI from 2.7 to 3.4 can be realized. The sensitivity and the average detection limit are 1.287 THz $R^{-1}IU^{-1}$ and 7.46×10^{-4} RIU. The figure of merit is up to 83.03 RIU^{-1}. Similarly, the structure is also competent to detect RI of another kind of dielectric layer from 2.2 to 2.85. The corresponding parameters are 1.241 THz RIU^{-1}, 7.12×10^{-4} RIU, and 77.53 RIU^{-1}, respectively. Meanwhile, the effects of the incident angle and machining inaccuracies are also discussed.

1. Introduction

Coherent perfect absorbers are devices in which two incident waves in opposite directions interfere with each other internally and interact with lossy materials where perfect absorption can be achieved [1, 2]. Coherent perfect absorption (CPA) is not only about achieving complete absorption of the incident wave. The absorption capacity of the devices that achieve CPA can also be flexibly controlled by adjusting the phases of the incident waves. Theoretically, the absorption can vary from 0% to 100% by artificial tuning. Such a tuning property is valued at the moment, as it does not depend on specific materials. In recent years, metamaterials have been made to exhibit tunability with the use of phase-change materials, such as GeSnTe and vanadium dioxide [3, 4]. By contrast, CPA can be achieved in multiple materials and geometries. Chong *et al* [1] demonstrated CPA with the use of the silicon slab. Guo [5] achieved CPA based on a metasurface made of black phosphorus. Shen *et al* [6] obtained CPA using a grating composed of gallium arsenide and air. This demonstrates the potential of CPA in combination with the properties of other materials. The flexible tunability allows CPA to be applied to optical switches and modulators [7]. Compared with the conventional dynamic modulation achieved with bulky structures or materials, devices based on CPA are compact and have potential applications in optical computing and photonic chips [8].

However, since CPA is essentially the time-reversed process of lasing [1], it is difficult to achieve CPA over a wide frequency band. Bandwidth has always been an important reference for the performance of absorbers. Thus, with narrow bandwidth, it is hard for CPA to be implemented in fields such as electromagnetic stealth and photovoltaic cells. Much effort has been made to increase the bandwidth of CPA. One solution that has

theoretically proven to be effective is the use of the white-light cavity which can provide the ideal resonance phase conditions over a frequency band [9]. There is also research that investigated broadband CPA theoretically and observed the corresponding phenomena in experiments on a metal-dielectric metamaterial [10]. Meanwhile, a metasurface embedded with unit cells was applied to provide multi-band CPA and the broadband CPA was achieved by optimizing the parameters on this basis [11]. Low-loss epsilon-near-zero films were also introduced to realize broadband CPA which are simple and scalable to implement [12]. However, most of the research about CPA mentioned above only focuses on the absorption performance without considering the tunability of CPA. Compared to the known one-side perfect absorption, two-port CPA which depends on the relationship between the incident lights applies to optical switches and all-optical logic gates [13–15].

As mentioned above, many materials have been applied to achieve CPA. Yet, ferrites are rarely mentioned in research related to CPA. Ferrites are magnetic dielectrics with which electromagnetic (EM) waves can interact when passing through [16]. Ferrites display special permeability in different magnetization configurations. Excellent anisotropy and tunability are brought about when the ferrite defects are introduced into the optical cavity. Bi *et al* investigated ferrite-based metamaterials and found that modifying the magnetic field applied to the ferrite can modulate the dielectric properties of the metamaterial [17]. A magnetically tunable terahertz (THz) circulator based on silicon and ferrite is proposed by Fan *et al* [18]. This shows that the tunability of ferrites is widely valued by researchers.

As is mentioned above, there is work on applying CPA to sensors and also on implementing broadband CPA. But there is hardly any research that uses the mechanism of CPA to achieve functional switching and much less work that implements CPA with wider bandwidth and the very narrowband CPA on the same device which can be used as an absorber and a sensor. Based on this, our goal is to design a structure achieving CPA and exploit the controllability of CPA to realize the functional switching, which is rarely addressed in research. In this work, we propose an optical device by introducing ferrite defects into the photonic crystals (PCs) [19–22] to form the optical cavity. PCs are multilayered structures of stacked layers of dielectrics with different refractive index (RI) values, which have special effects on the propagation of light. Fabry-Pérot (FP) cavity is the most commonly used structure to achieve CPA, in which incident light can bounce back and forth. It can enhance the absorption capacity of the whole structure. By introducing ferrite defect layers, the spectra of the PCs are altered and the optical cavity is endowed with tunable properties. The purpose is not only to increase the bandwidth of CPA but also to enable functional switching with the advantage of the tunability of CPA. Ultimately, an optical device with functional switching characteristics is proposed. The presented structure can be switched between a narrowband absorption function and a sensing function by altering the phase difference of the incident lights. The relative bandwidth (RBW) of the absorption band is 9.7%. And the maximum absorptance does not fall below 0.8 until the incident angle increases to 68°. The quality (Q) value of the absorption peak is modulated to 494.85 by altering the magnetic field applied in the ferrite layers, which indicates the potential for use as a sensor. The highly linear relationships can be found between the RI values of dielectric layers and the spike absorption frequencies. The accurate analysis of the RI from 2.7 to 3.4 can be realized. The sensitivity (S) and the average detection limit (DL) are 1.287 THz $R^{-1}IU^{-1}$ and 7.46×10^{-4} RIU. The figure of merit (FOM) is up to 83.03 RIU^{-1}. Similarly, the structure is also competent to detect RI of another kind of dielectric layer from 2.2 to 2.85. S and average DL are 1.241 THz/RIU and 7.12×10^{-4} RIU. The maximum FOM is 77.53 RIU^{-1}. There are few cases of CPA for use for sensing and there is little research on expanding the bandwidth of CPA, not to mention combining the two functions in a single device. The proposed structure implements these two functions from a rather novel perspective, which provides innovative insights for further applications of CPA.

2. Simulation model and formulation

The structure of the proposed optical cavity is shown in figure 1, where A, B, C, and D represent four common materials with different RI values. Here PCs resonant cavities $(AB)^2$-F_1-F_2-(ABCAB)-D-(BACBA)-F_2-F_1-$(BA)^2$ are utilized to provide an absorption spike with a high Q value. The resonant cavity formed by the laminated structure results in a narrow spectral width. And the ferrite layers inserted in it help to adjust the Q value. Therefore, in sensing mode, such a structure provides higher sensor accuracy and an overall improvement in sensor performance. Ferrite material Yttrium iron garnet (YIG) is used for defect layers, which is often introduced into structures in this way in theoretical research [23–25]. The two kinds of defect layers, which are represented as Ferrite1 and Ferrite2 respectively, are both made of YIG. However, the magnetic fields applied to them are of different magnitudes and in opposite directions, denoted as H_{01} and H_{02} respectively. H_{01} is oriented in the same direction as the $+z$-axis, while H_{02} is oriented along the $-z$-axis. The directions are marked with arrows in figure 1. Thicknesses of the dielectric layers are signified with $d_A = 4.6$ μm, $d_B = 8.7$ μm, $d_C = 23.4$ μm, $d_D = 9$ μm, $d_{F1} = 6.8$ μm and $d_{F2} = 5$ μm. The thickness is selected according to the operating frequency band and absorption efficiency. The thickness in the millimeter range allows the operating band to be located in the terahertz band. Both incident waves propagate in the *xoy* plane and the angle of incidence is expressed as θ. The

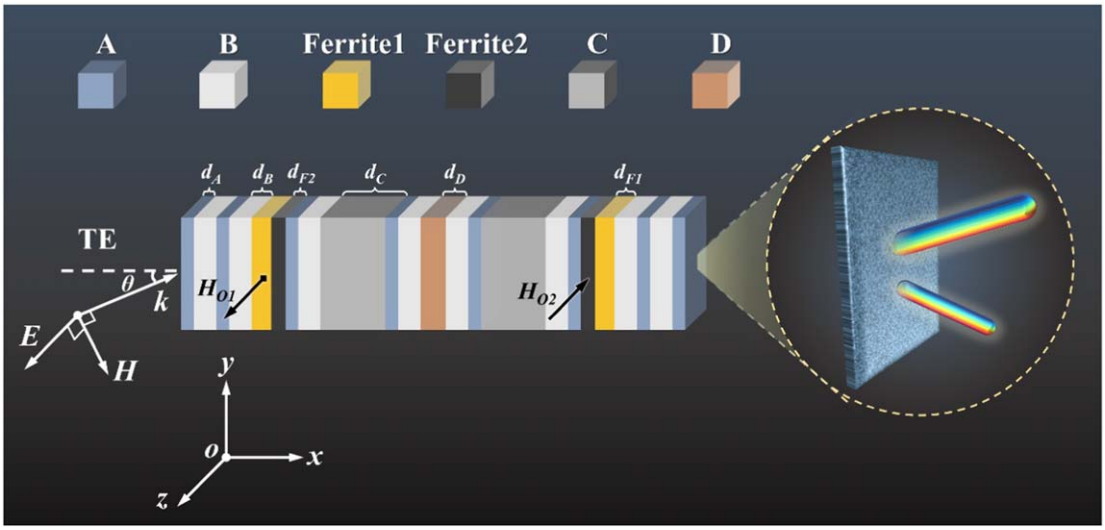

Figure 1. Schematic diagram of the proposed optical cavity with ferrite defects.

overall structure is based on the FP cavity, with defect layers introduced in the form of replacements or inserts. This is reasonable, as a single FP cavity often needs to optimize all parameters of each layer to obtain the desired effect of absorption. By introducing defective layers, the spectrum of the structure can be modulated by the defect layers, especially the ferrite layers, thus making the process much easier. Meanwhile, the RIs of materials are different which are expressed as $n_A = 2.17$, $n_B = 3$, $n_C = 2.5$ and $n_D = 2.3$, to be specific. The permittivity of the ferrite layers is taken as $\varepsilon_{F1} = \varepsilon_{F2} = \varepsilon_m = 15$ according to previous research [26]. It is worth mentioning that our work is theoretical research, the requirement is that the materials constituting the structure should have these specific refraction indices in the terahertz band as we have chosen. How to manufacture or experimentally implement the materials is not in the scope of the discussion. There are many precedents in theoretical analysis where the intrinsic absorbance is negligible because of the small imaginary part of the permittivity of the material, so we make the same proposal in this work. The proposed materials have sufficiently small imaginary parts. The chosen parameters are not unattainable, considering that the RI of silicon is about 3.42 at terahertz frequencies and the RI of silicon dioxide is about 2.12 at terahertz frequencies [27, 28]. On the other hand, the structure we propose is not completely unattainable if the experimental implementation is considered. Deposition and etching are common methods used to manufacture the structure [29] and the YIG films have been fabricated and applied to PCs in the published work [30].

The transfer matrix for the entire optical cavity is first deduced with the transfer matrix method (TMM)[23], which is the basis for the subsequent simulations. As for YIG, the effective permeability is a tensor in the transverse magnetization configuration, which can be expressed as [31]

$$\hat{\boldsymbol{\mu}}_{\boldsymbol{m}} = \begin{pmatrix} \mu_r & 0 & j\mu_k \\ 0 & \mu_0 & 0 \\ -j\mu_k & 0 & \mu_r \end{pmatrix}, \tag{1}$$

$$\mu_r = 1 + \frac{\omega_m(\omega_0 - j\alpha\omega)}{(\omega_0 - j\alpha\omega)^2 - \omega^2}, \tag{2}$$

$$\mu_k = \frac{\omega_m\omega}{(\omega_0 - j\alpha\omega)^2 - \omega^2}. \tag{3}$$

Here, $\alpha = 0.02$ refers to the damping coefficient [24]. ω_0 is the resonance frequency, with the form as $\omega_0 = 2\pi\gamma H_0$, where $\gamma = 2.8$ GHz Oe^{-1} is the gyromagnetic ratio [24] and H_0 is the intensity of the magnetic field. In this work, H_{01} and H_{02} are modulated to realize different functions. The circular frequency of YIG is represented as $\omega_m = 2\pi\gamma M_S$, where M_S is the saturation magnetization and taken as $M_S = 1780$ Oe, which is a typical value [24].

The effective RI of YIG under the transverse electric (TE) polarization is [26]

$$n_{YIG} = \sqrt{\frac{{\mu_r}^2 + (j\mu_k)^2}{\mu_r} \cdot \varepsilon_{YIG}}. \tag{4}$$

It is well known that ferrites are unaffected by the applied magnetic field under a transverse magnetization (TM) configuration. In this work, magnetic field modulation has a critical impact on the performance of the

proposed structure. Hence, we concentrate on the transfer properties of the ferrite layer in TE mode in the following discussion.

Utilizing Maxwell curl equations and considering the boundary conditions of the EM wave propagating in the dielectric layer, the transfer matrix of the ferrite layer can be deduced [26]

$$\boldsymbol{M_{TE}} = \begin{pmatrix} \cos(k_{TEx}d_i) + \sin(k_{TEx}d_i)\cdot\dfrac{k_{TEy}\mu_k}{k_{TEx}\mu_r} & -\dfrac{j}{\eta_{TE}}\left[1+\left(\dfrac{k_{TEy}\mu_k}{k_{TEx}\mu_r}\right)^2\right]\cdot\sin(k_{TEx}d_i) \\ -j\eta_{TE}\cdot\sin(k_{TEx}d_i) & \cos(k_{TEx}d_i) - \sin(k_{TEx}d_i)\cdot\dfrac{k_{TEy}\mu_k}{k_{TEx}\mu_r} \end{pmatrix}, \tag{5}$$

where $\eta_{\mathrm{TE}} = (\mu_0/\varepsilon_0)^{1/2}\cdot([\mu_r^2+(j\mu_k)^2]/(\varepsilon_m\mu_r))^{1/2}/\cos\theta_f$, $k_{\mathrm{TE}} = (\omega/c)\{(\varepsilon_m/\mu_r)\cdot[\mu_r^2+(j\mu_k)^2]\}^{1/2}$, $k_{\mathrm{TE}y} = k_{\mathrm{TE}}\sin\theta_f$, $k_{\mathrm{TE}x} = k_{\mathrm{TE}}\cos\theta_f$, and θ_f is the refractive angle of the ferrite layers.

For the common dielectric layers, the transfer matrix can be expressed as [32]

$$\boldsymbol{M_i} = \begin{pmatrix} \cos\delta_i & -j\sin\delta_i/\eta_i \\ -j\eta_i\sin\delta_i & \cos\delta_i \end{pmatrix} (i = \mathrm{A},\ \mathrm{B},\ \mathrm{C},\ \mathrm{D}) \tag{6}$$

where $\eta_i = (\varepsilon_0/\mu_0)^{1/2} n_i\cos\theta_i$ and δ_i is the propagating phase which is expressed as $\delta_i = n_i d_i\cos\theta_i(2\pi/\lambda)$. Here symbols are added with subscript i to represent the parameters of the different layers.

The overall transfer matrix of the entire structure can be derived recursively from the transfer matrix of the individual dielectric layers and the arrangement of the cavities. This is shown as follows [32]

$$\begin{pmatrix} E_1 \\ H_1 \end{pmatrix} = [(\boldsymbol{M_A M_B})^2\boldsymbol{M_{F1}M_{F2}M_A}\cdots\boldsymbol{M_{F1}}(\boldsymbol{M_B M_A})^2] \cdot\begin{pmatrix} E_{N+1} \\ H_{N+1} \end{pmatrix} = \begin{pmatrix} m_{11} & m_{12} \\ m_{21} & m_{22} \end{pmatrix}\cdot\begin{pmatrix} E_{N+1} \\ H_{N+1} \end{pmatrix} \tag{7}$$

Via the transfer matrix derived above, the reflection coefficient and transmission coefficient can be expressed as [32]

$$r = \frac{(m_{11}+m_{12}\eta_{N+1})\eta_0 - (m_{21}+m_{22}\eta_{N+1})}{m_{11}\eta_0 + m_{12}\eta_0\eta_{N+1} + m_{21} + m_{22}\eta_{N+1}}, \tag{8}$$

$$t = \frac{2\eta_0}{m_{11}\eta_0 + m_{12}\eta_0\eta_{N+1} + m_{21} + m_{22}\eta_{N+1}}. \tag{9}$$

And $\eta_0 = \eta_{\mathrm{N}+1} = (\varepsilon_0/\mu_0)^{1/2}\cos\theta_0$ because the light is incident from the air in TE mode in this work.

Hence, the reflectance, transmittance, and absorptance of the whole structure can be obtained:

$$R = |r|^2, \tag{10}$$

$$T = |t|^2, \tag{11}$$

$$A = 1 - |r|^2 - |t|^2. \tag{12}$$

This is followed by a description of the conditions for CPA. The generation condition for CPA is then obtained by numerical derivation and is of guidance in achieving CPA and modulating the absorption.

A schematic diagram of the CPA is shown in figure 2. Two coherent beams are directed in opposite directions into the absorber, one from the front (I_+) and and the other from the back (I_-). In this work, the absorber is of a symmetric structure. An incident light produces a reflected light and a transmitted light. Scattered waves (O_+ and O_-) can be detected at the front and rear sides of the absorber, containing lights reflected from the same side and transmitted from the other side. The input and output waves are connected by a scattering matrix [33]

$$\begin{pmatrix} O_+ \\ O_- \end{pmatrix} = \boldsymbol{S}\begin{pmatrix} I_+ \\ I_- \end{pmatrix} = \begin{pmatrix} t_+ & r_- \\ r_+ & t_- \end{pmatrix}\begin{pmatrix} I_+ \\ I_- \end{pmatrix}, \tag{13}$$

where the transmission and reflection coefficients of two sides are respectively represented as (t_+, r_+) and (t_-, r_-). Because of the symmetry of the structure, the transmission coefficients are numerically equal and reflection coefficients are also numerically the same, which can be described as $t_+ = t_- = t$, $r_+ = r_- = r$. Consequently, the scattered waves are denoted as [33]

$$O_+ = t|I_+|\ e^{i\phi_+} + r|I_-|\ e^{i\phi_-}, \tag{14}$$

$$O_- = r|I_+|\ e^{i\phi_+} + t|I_-|\ e^{i\phi_-}, \tag{15}$$

Here, ϕ_+ and ϕ_- are the symbols of the phases of two waves of incidence.

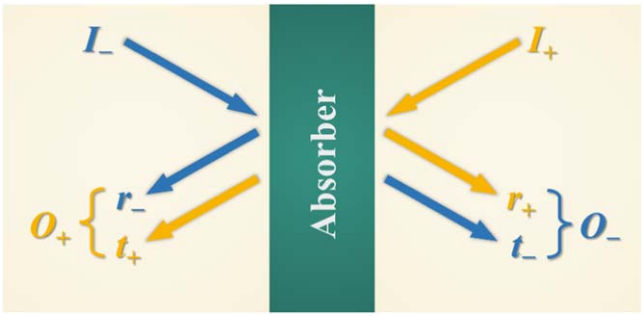

Figure 2. The schematic diagram of the system of CPA.

As a result, the CPA can be expressed by the intensities of input and output lights

$$A_C = 1 - \frac{|O_+|^2 + |O_-|^2}{|I_+|^2 + |I_-|^2}, \tag{16}$$

It can be further written as:

$$A_C = 1 - (|t| - |r|)^2 - 2|t||r|\left(1 + \frac{2|I_+||I_-|\cos\Delta\phi_1\cos\Delta\phi_2}{|I_+|^2 + |I_-|^2}\right), \tag{17}$$

where $\Delta\phi_1 = \mathrm{Arg}(t) - \mathrm{Arg}(r)$ is the difference in phase of transmission and reflection coefficients and the difference in phase of two incident waves $\Delta\phi_2 = \phi_+ - \phi_-$.

Equation (17) indicates the conditions of CPA. Intuitively, when a beam of light is incident without correspondingly producing transmitted and reflected light, this phenomenon can be described as perfect absorption, which means $|t| = |r| = 0$. In this condition, equation (17) equals 1, confirming this inference. Nevertheless, for the vast majority of situations, the materials and structures do not meet this condition. Meanwhile, the other conditions can be found by observing the equation, which are $|I_+| = |I_-|$, $|t| = |r|$, and $\cos\Delta\phi_1\cos\Delta\phi_2 = -1$. It can be known that if the two light is controlled to be of the same intensity, the transmittance is equal to the reflectance with $\Delta\phi_1 = 0$, the only variable that can affect the absorptance is $\Delta\phi_2$. In other words, the absorptance can be modulated by altering the phase difference between two incident lights.

3. Analysis and discussion

3.1. The switch between the narrowband absorption and the spike absorption

In the following section, the intensities of the two incident beams are set to be the same. Setting $H_{01} = 7337$ Oe and $H_{02} = -5640$ Oe, CPA can be found at specific frequencies. In the range of 6.9 to 8 THz, a narrow absorption band is generated when $\Delta\phi_2 = 180°$. While a sharp absorption peak arises at $\Delta\phi_2 = 0°$ with the disappearance of the narrow absorption band. The absorption curves at these two phases are drawn in figure 3. Meanwhile, figure 4 is drawn to visually demonstrate the role of $\Delta\phi_2$ in functional switching and to improve the existence of CPA. The two phenomena appear alternately with the modulation of CPA.

3.2. The narrowband absorption

The narrowband absorption is first to be discussed. The narrowband absorption is attributed to the proximity of the three absorption peaks. As illustrated in figure 4(a), reflectance and transmittance oscillate up and down between 7 and 7.78 THz, and are found to be equal at 7.01THz, 7.13 THz, 7.31 THz, 7.50 THz, 7.70 THz, and 7.78 THz, respectively. The cosine value of $\Delta\phi_1$ equals 1 at 7.07 THz, 7.38 THz, and 7.73 THz. These phenomena are consistent with the conditions of CPA. As a result, the absorptance reaches maximums at 7.08 THz, 7.38THz, and 7.73THz, which are 0.960, 0.996, and 0.998, respectively. The absorption bandwidth is 0.718 THz and RBW is 9.7%. Figure 5 depicts how the absorption changes with $\Delta\phi_2$, showing that modulating the phase merely changes the absorptance and does not result in a frequency shift.

Impacts of the incident angle on the absorption of the structure are exhibited, as shown in figure 6, when $\Delta\phi_2 = 180°$, the bandwidth of absorption above 80% does not change much until the incidence angle is over 56°, after which the bandwidth is halved. Starting at $\theta = 4°$, the middle part of the absorption band becomes concave and falls below 90% as the angle increases. As an optical precision device, the input lights were set to be

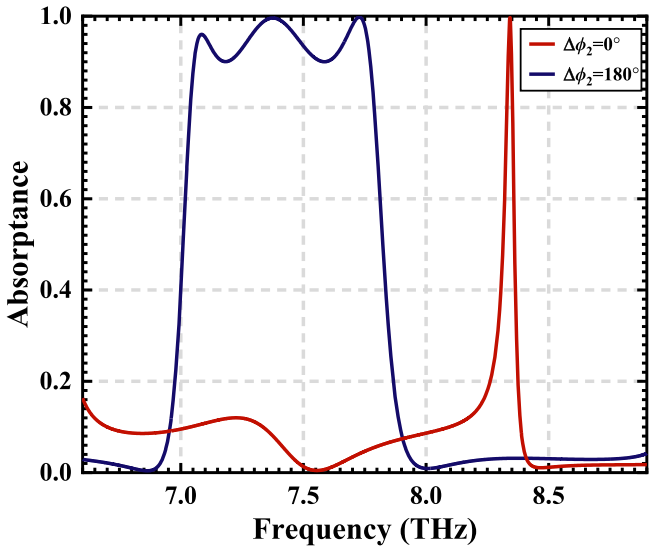

Figure 3. The absorption curves at different phases between incident lights. The proposed structure exhibits narrowband absorption at $\Delta\phi_2 = 180°$ and spike absorption at $\Delta\phi_2 = 0°$.

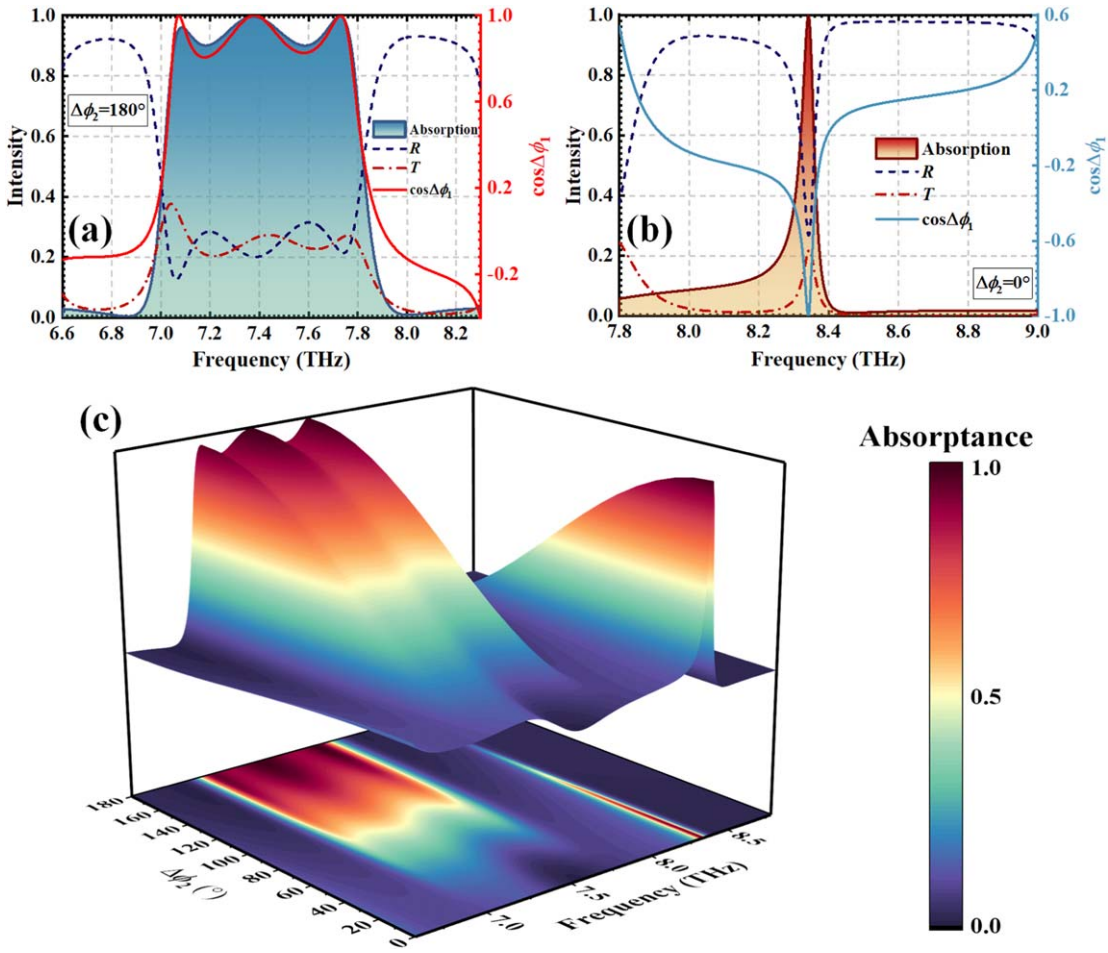

Figure 4. Transmittance, reflectance, and the phase difference $\Delta\phi_1$ versus frequency for (a) the narrowband absorption and (b) the absorption peak. (c) The three-dimensional (3D) surface plot of absorptance variation with $\Delta\phi_2$ and frequency.

vertically incident to the structure for the best absorption performance. The result shown in the figure indicates the robustness of the structure. The maximum absorptance does not fall below 80% until the incidence angle is 68°. With the increase of θ, the absorption band has a blue-shift phenomenon.

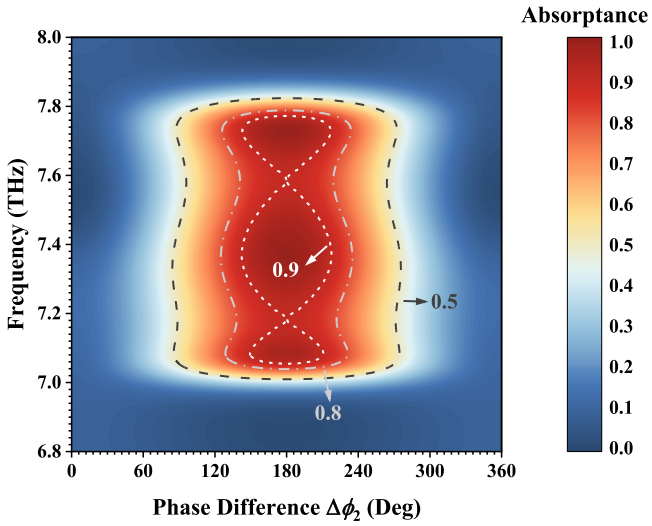

Figure 5. The variation of narrowband absorptance with the phase difference between the two incident lights.

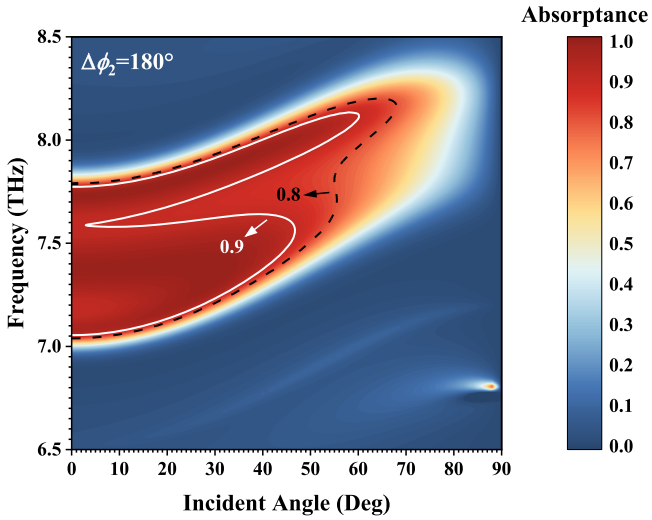

Figure 6. CPA as a function of incident angle and frequency. Ideal absorption areas where CPA $\geqslant$ 0.9 and CPA $\geqslant$ 0.8 are marked out by white solid lines and black dashed lines separately.

Due to the demanding conditions of CPA, especially, for narrowband absorption, it is necessary to discuss the tolerance for the parameters of the device. After research, it is found that the changes in device parameters have a similar effect on the absorption band. Taking d_A as an example, the variation of absorption is shown in figure 7. It can be observed in figure 7(a) that the absorption band does not shift obviously in frequency when $\Delta\phi_2 = 180°$. However, one side of the absorption band falls with the variation of d_A. The side with high frequency begins to fall below 80% when d_A is less than 4.52 μm and the other side begins to fall below 80% when d_A is more than 4.68 μm. This indicates that achieving narrowband absorption requires precise parameter selection. By contrast, from figure 7(b), when $\Delta\phi_2 = 0°$, the frequency of the spike absorption shifts slightly (8.3745 ~ 8.3190 THz) with the variation of d_A, and the spike absorptance remains over 0.9 during this process.

3.3. The sensing performance

When the phases of the two incident waves are adjusted to coincide, the absorption band disappears and an absorption peak is observed at 8.342 THz, which can be seen in figure 4(c). R, T, and $\Delta\phi_1$ as functions of frequency are shown in figure 4(b). R is 0.2689, T is 0.2171 and the cosine value of $\Delta\phi_1$ is -1 at 8.342 THz. As a result of this, an absorption peak appears at the same frequency with the absorptance of 0.997. The prospect of using this as a basis for a sensor will be discussed.

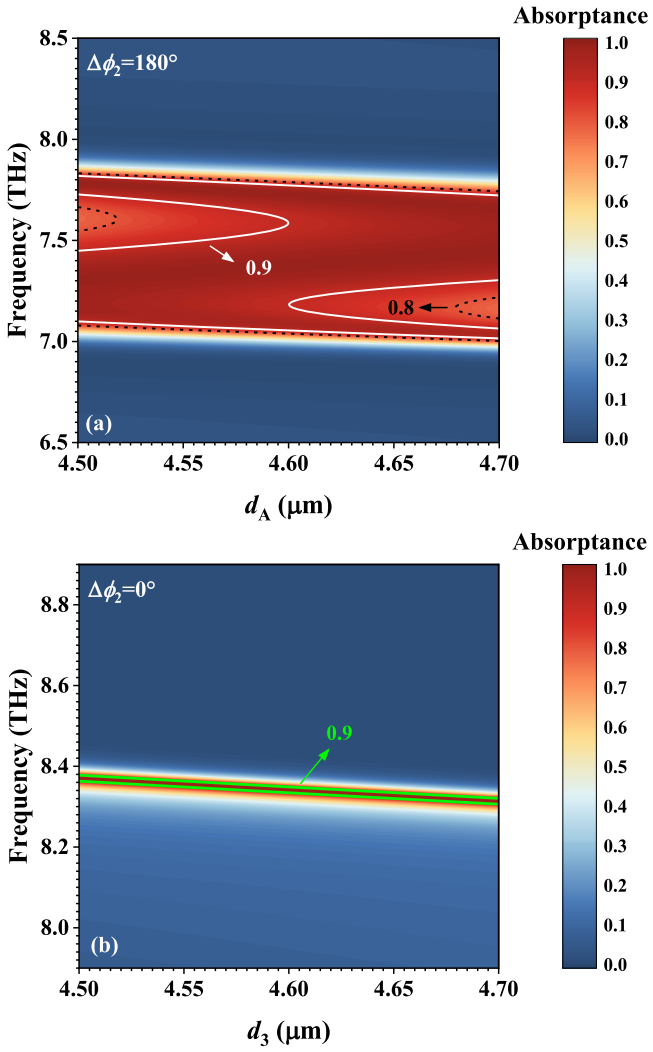

Figure 7. (a) The variation of the absorption band with d_A. CPA = 0.9 and CPA = 0.8 are marked out by white solid lines and black dashed lines, respectively. (b) The variation of the absorption peak with d_A. CPA = 0.9 are marked out by green solid lines and black dashed lines, respectively.

In this paper, all of the dielectric layers are seen as a whole structure. But when used as a sensor, some of these dielectric layers are filled with the substances to be measured. This work is to present a new structure with attractive performance and discuss it theoretically sharing innovative ideas. But if practical applications are considered, it is also feasible to put our theory into practice. In preparation of the structure, a common method is etching. The structure can be formed by etching out vertical grooves and filling them with the corresponding substances according to the design [29]. When the structure is used as a sensor, the corresponding positions of those layers are vacant. For gases and liquids to be measured, the structure can be placed in an environment filled with the substance to be measured, with the air layer at both ends as light incidence ports. For solids, thin films of these kinds of substances of the same size can be grown and inserted into the structure or stacked with other media layers of the structure.

To evaluate a sensor, several parameters should be introduced, which are Q, S, FOM, and DL. The Q value is defined as the ratio of the resonant absorption frequency f_T versus the full width at half maximum (FWHM) of the resonant absorption peak. S is used to measure the ability of a sensor to respond to changes in the measured value. FOM is defined as the ratio between S and FWHM, which is a parameter to measure the comprehensive performance of a sensor [34]. DL describes the minimal change of RI that can be detected by the sensor [35].

$$Q = \frac{f_T}{FWHM} \tag{18}$$

$$S = \frac{\Delta f}{\Delta n} \tag{19}$$

$$FOM = \frac{S}{FWHM} \tag{20}$$

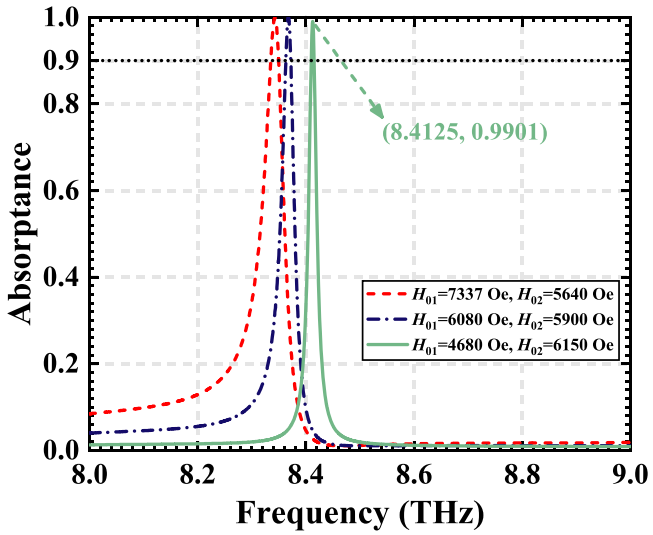

Figure 8. Modulation of the absorption peak by the magnetic field. The absorption bandwidth is narrower and the absorption peak is steeper by magnetic field modulation.

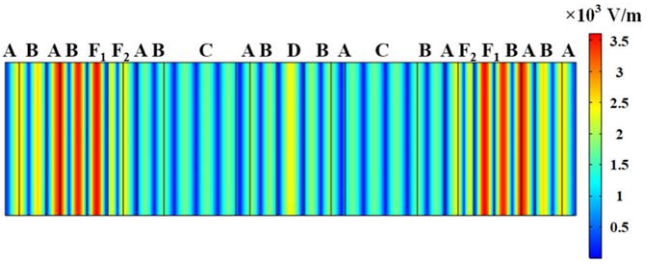

Figure 9. The distribution of electric field at 8.4125 THz.

$$DL = \frac{f_T}{20 \cdot S \cdot Q} \tag{21}$$

where Δf and Δn are the changes of frequency and RI respectively.

As a dual-function device, it is not easy to get multiple functions to perform well at the same time. But the single function can be made to perform better by changing the configuration of the magnetic field applied in the ferrite layers. As shown in figure 8, the bandwidth of the absorption peak is further narrowed by altering the magnetic field and the performance of the sensor will be improved consequently. It means that, without changing the structure or materials, the function can be switched by optical phase modulation, and then the single function that is operating can perform better via magnetic field modulation, a non-contact mean. If considering the actual operation, the magnetic field can be generated by an energized gradient coil [36], which is a spatial linear magnetic field suitable for use in this proposed structure. A spatial linear magnetic field can be generated with gradient magnetic field coils. Setting $H_{01} = 4680$ Oe and $H_{02} = -6150$ Oe, the absorption peak becomes sharper and the Q value is 494.85, which used to be 175.62. The peak is at 8.4125 THz and of absorptance of 0.9901 after the modulation of the magnetic field. Compared to the absorption peak before adjustment, the spike shifts slightly towards the high frequency, but the Q value increases substantially and the spike absorptance remains above 0.99.

When the frequency is 8.4125 THz, the electric field distribution is shown in figure 9. It can be seen that the energy is mainly concentrated in the ferrite layers, which is due to the periodic arrangement of the common dielectric layers forming pairs of FP cavities with the ferrite layers in the middle, where the light is continuously reflected in the FP cavities and the energy is dissipated in the ferrite layer. This explains where the energy of CPA goes.

Maintaining the magnetic field configuration above, the ability of the proposed structure to measure the RI was investigated. Figure 10(a) shows the absorption curves produced at different RI. With n_B changing from

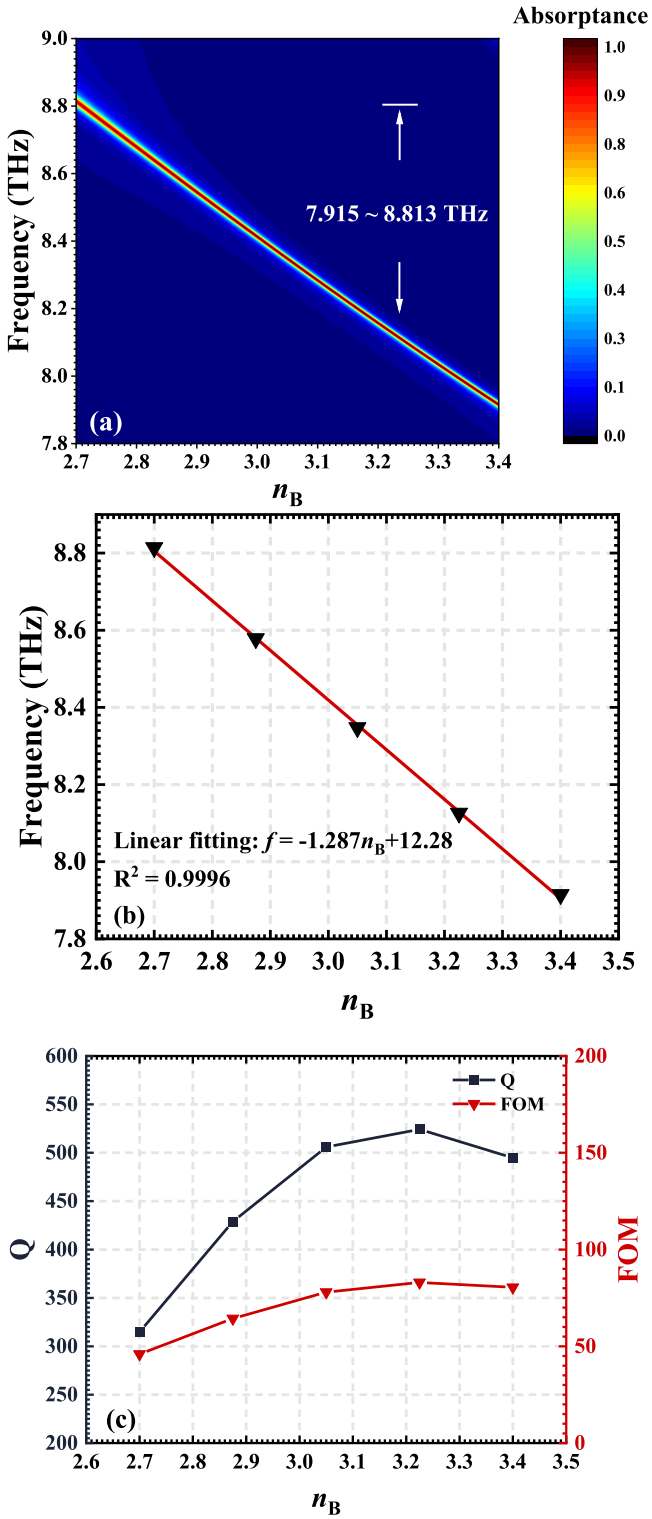

Figure 10. (a) The absorption spectra in sensing function mode versus n_B. (b) The linear relationship between the RI and resonance absorption frequency. (c) Q and FOM changing with RI.

2.7 to 3.4, the frequency of absorption spike varies from 8.813 to 7.915 THz, showing a highly linear relationship with RI. This is because the variation in RI will result in a change in the wavelength of the light propagating through the medium. This can cause a change in the phase of the two coherent waves when they interact in the medium, resulting in a reduction in the absorption of those waves that could be perfectly absorbed in the original frequency. The frequency at which CPA is achieved will therefore change as the RI varies. The results of the curve fitting are plotted in figure 10(b). As n_B isometrically increases from 2.7 to 3.4, the frequencies of the absorption peaks are 8.814 THz, 8.575 THz, 8.3475 THz, 8.126THz, and 7.915 THz respectively. Within this range, the relationship between n_B and frequency can be expressed as a linear fitting equation, which is $f = -1.287n_B + 12.28$

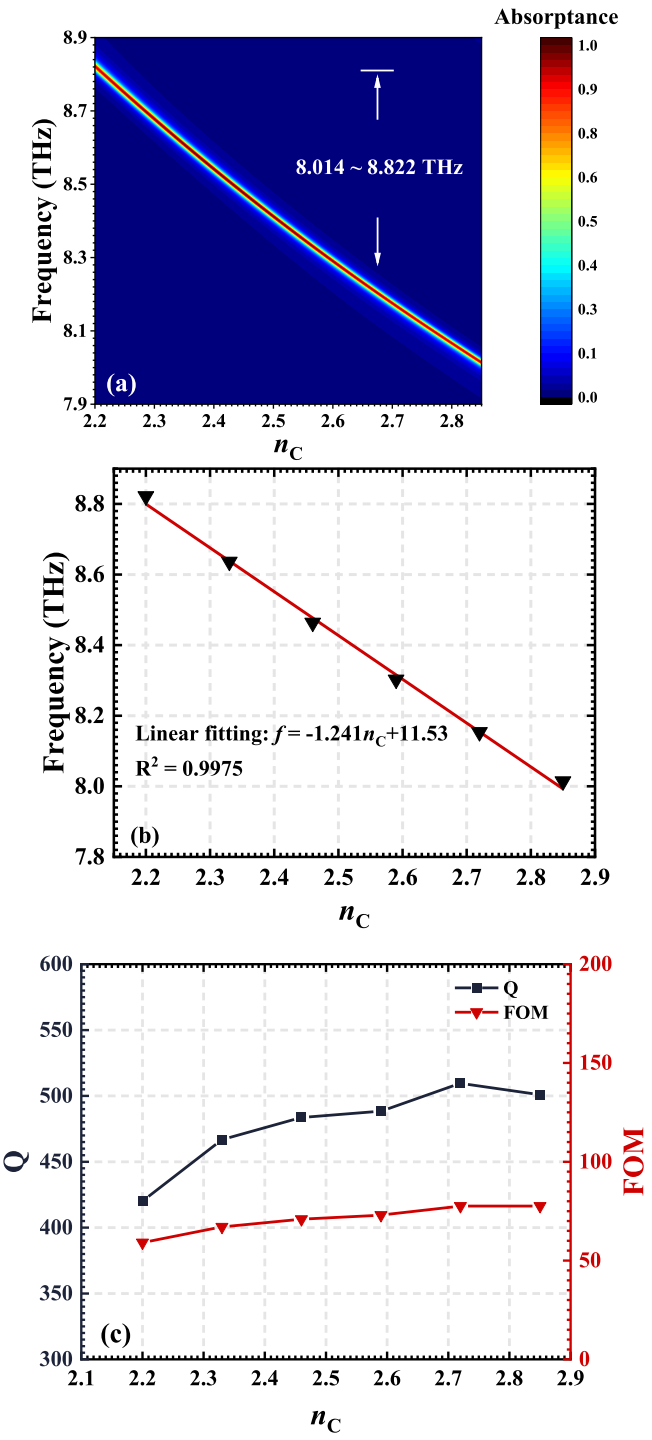

Figure 11. (a) The absorption spectra in sensing function mode versus n_C. (b) The linear relationship between the RI and resonance absorption frequency. (c) Q and FOM changing with RI.

with $R^2 = 0.9996$. S is 1.287 THz $R^{-1}IU^{-1}$ according to the equation. As the RI changes, the Q value can be up to 524.26 and the lowest is 314.78, and FOM is at a maximum of 83.03 RIU^{-1} and a minimum of 45.96 RIU^{-1}, which can be observed in figure 10(c). The average DL of 7.46×10^{-4} RIU can be calculated according to equation (17). All of the above parameters indicate that the proposed structure has decent sensing properties.

The same principle can be applied to measure the n_C. Figure 11(a) displays the color mapping plan of absorption generated at different RI. When n_C varies from 2.2 to 2.85, the frequency of absorption spike is 8.813 ~ 7.915 THz. The fitted curve is plotted in figure 11(b). As n_C incrementally expands from 2.2 to 2.85, the frequencies of the absorption peaks are 8.822 THz, 8.636 THz, 8.464 THz, 8.302THz, 8.154 THz, and 8.014 THz respectively. A linear fitting equation can be obtained, which is $f = -1.241n_C + 11.53$ with $R^2 = 0.9975$, meaning that S is 1.241 THz/RIU. As shown in figure 11(c), the maximum and minimum of Q are 509.59 and 420.10, and

Table 1. Comparison of other research and this work.

Performance	Reference [10]	Reference [11]	Reference [30]	This work
Phase modulation	Yes	Yes	No	Yes
Magnetic field modulation	No	No	No	Yes
Dual-function	No	No	No	Yes
RBW	~10%	5.5% (101.7 ~ 107.4 THz)	—	9.7% (7.05 ~ 7.77 THz)
Measuring range	—	—	2.0 ~ 2.7	2.2 ~ 2.85, 2.7 ~ 3.4
S	—	—	32.3 THz/RIU	1.287 THz/RIU, 1.241 THz/RIU
FOM	—	—	100	70.9, 70.4

those of FOM are 77.53 RIU^{-1} and 59.10 RIU^{-1}, respectively. Then the average DL of 7.12×10^{-4} RIU can be calculated.

Any conventional dielectric material with refractive indices in this range can be detected with the proposed structure. However, slightly changing the RI values of other dielectric layers, the frequency shift of the absorption peak does not show a good linear relationship with the variation of RI values, or the intensity of the absorption peak decreases sharply with the change of RI values, both of which are detrimental to the operation of the sensor. This is because changes in the RI values of these materials have a significant effect on the system response and can easily make the absorber deviate from the CPA conditions.

The traditional device usually only has one function and in most cases what makes it special is the extreme performance in one specific indicator [10, 11, 37]. By contrast, the structure proposed in this work is born under a novel research direction. The thought that realizing two functions in one structure is of practical relevance nowadays. The results of this study show that the proposed structure has good performance in both functions. Table 1 is shown for comparison to have an intuitive appreciation of the advantages of our design.

4. Conclusion

In this work, an optical structure with a narrowband absorption feature and sensing performance is proposed. But more importantly, these two features can be switched by optical phase modulation. Both of the two features are analyzed with the TMM. Via the switching characteristics of CPA, the narrowband absorption feature and the sensing function occur alternately. When the phase of the two incident lights is adjusted to the same, a spike absorption can be obtained and have potential as a sensor. When adjusting the phase of the two incident lights to be opposite, the absorption peak disappears and a narrow absorption band arises. The RBW of the absorption band is 9.7%. When measuring the RI of one kind of dielectric layer from 2.7 to 3.4, S and the average DL are 1.287 THz $R^{-1}IU^{-1}$ and 7.46×10^{-4} RIU respectively. The maximum FOM is up to 83.03 RIU^{-1}. When it is used for the measurement of the RI of another kind of dielectric layer from 2.2 to 2.85, S and average DL are 1.241 THz/RIU and 7.12×10^{-4} RIU. FOM is up to 77.53 RIU^{-1} at maximum. The effects of θ and d_A on narrowband absorption are discussed. And the influence of H_{02} on the sensing performance is also discussed briefly. The structure is simple and easy to implement, and the dual-function is suitable for a wide range of potential applications.

Data availability statement

The data generated and/or analysed during the current study are not publicly available for legal/ethical reasons but are available from the corresponding author on reasonable request.

ORCID iDs

Haifeng Zhang https://orcid.org/0000-0002-9890-8345

References

[1] Chong Y D, Ge L, Cao H and Stone A D 2010 Coherent perfect absorbers: time-reversed lasers *Phys. Rev. Lett.* **105** 053901
[2] Wan W, Chong Y, Ge L, Noh H, Stone A D and Cao H 2011 Time-reversed lasing and interferometric control of absorption *Science* **331** 889–92
[3] Cao T, Wei C, Simpson R E, Zhang L and Cryan M J 2014 Broadband polarization-independent perfect absorber using a phase-change metamaterial at visible frequencies *Sci. Rep.* **4** 3955

[4] Liu L, Kang L, Mayer T S and Werner D H 2016 Hybrid metamaterials for electrically triggered multifunctional control *Nat Commun* **7** 13236
[5] Guo T and Argyropoulos C 2019 Tunable and broadband coherent perfect absorption by ultrathin black phosphorus metasurfaces *J. Opt. Soc. Am. B, JOSAB* **36** 2962–71
[6] Shen Y, Shen L, Lai Z, Wang G and Deng X 2014 Time-reversed lasing based on one-dimensional gratings *Phys. Lett. A* **378** 299–302
[7] Bruck R and Muskens O L 2013 Plasmonic nanoantennas as integrated coherent perfect absorbers on SOI waveguides for modulators and all-optical switches *Opt. Express, OE* **21** 27652–61
[8] Lipson M 2005 Guiding, modulating, and emitting light on Silicon-challenges and opportunities *J. Lightwave Technol.* **23** 4222–38
[9] Kotlicki O and Scheuer J 2014 Wideband coherent perfect absorber based on white-light cavity *Opt. Lett., OL* **39** 6624–7
[10] Baldacci L, Zanotto S, Biasiol G, Sorba L and Tredicucci A 2015 Interferometric control of absorption in thin plasmonic metamaterials: general two port theory and broadband operation *Opt. Express, OE* **23** 9202–10
[11] Huang S, Xie Z, Chen W, Lei J, Wang F, Liu K and Li L 2018 Metasurface with multi-sized structure for multi-band coherent perfect absorption *Opt. Express, OE* **26** 7066–78
[12] Kim T Y, Badsha M A, Yoon J, Lee S Y, Jun Y C and Hwangbo C K 2016 General strategy for broadband coherent perfect absorption and multi-wavelength all-optical switching based on epsilon-near-zero multilayer films *Sci. Rep.* **6** 22941
[13] Ebrahimi Meymand R, Soleymani A and Granpayeh N 2020 All-optical AND, OR, and XOR logic gates based on coherent perfect absorption in graphene-based metasurface at terahertz region *Opt. Commun.* **458** 124772
[14] Papaioannou M, Plum E, Valente J, Rogers E T F and Zheludev N I 2016 All-optical multichannel logic based on coherent perfect absorption in a plasmonic metamaterial *APL Photonics* **1** 090801
[15] Papaioannou M, Plum E, Valente J, Rogers E T and Zheludev N I 2016 Two-dimensional control of light with light on metasurfaces *Light: Sci. Appl.* **5** e16070–16070
[16] Adam J D, Davis L E, Dionne G F, Schloemann E F and Stitzer S N 2002 Ferrite devices and materials *IEEE Trans. Microwave Theory Tech.* **50** 721–37
[17] Bi K, Huang K, Zeng L Y, Zhou M H, Wang Q M, Wang Y G and Lei M 2015 Tunable dielectric properties of ferrite-dielectric based metamaterial *PLoS One* **10** e0127331
[18] Fan F, Chang S-J, Niu C, Hou Y and Wang X-H 2012 Magnetically tunable silicon-ferrite photonic crystals for terahertz circulator *Opt. Commun.* **285** 3763–9
[19] Yablonovitch E 1987 Inhibited spontaneous emission in solid-state physics and electronics *Phys. Rev. Lett.* **58** 2059–62
[20] Winn J N, Fink Y, Fan S and Joannopoulos J D 1998 Omnidirectional reflection from a one-dimensional photonic crystal *Opt. Lett., OL* **23** 1573–5
[21] Wu F, Wu X, Xiao S, Liu G and Li H-J 2021 Broadband wide-angle multilayer absorber based on a broadband omnidirectional optical tamm state *Opt. Express* **29** 23976–87
[22] Wu F, Chen M, Xiao S and Xiao S 2022 Wide-angle polarization selectivity based on anomalous defect mode in photonic crystal containing hyperbolic metamaterials *Opt. Lett., OL* **47** 2153–6
[23] Guo S, Mao M, Zhou Z, Zhang D and Zhang H 2020 The wide-angle broadband absorption and polarization separation in the one-dimensional magnetized ferrite photonic crystals arranged by the Dodecanacci sequence under the transverse magnetization configuration *J. Phys. D: Appl. Phys.* **54** 015004
[24] Sharma Y, Prasad S and Singh V 2018 Dispersion behavior of electromagnetic wave near the resonance in 1D magnetized ferrite photonic crystals *Opt Quant Electron* **50** 410
[25] Guo S-J, Li Z-J, Li F-Y, Xu Y and Zhang H-F 2021 The asymmetric optical bistability based on the one-dimensional photonic crystals composed of the defect layers containing the magnetized ferrite and nonlinear Kerr dielectric under the transverse electric polarization *J. Appl. Phys.* **129** 093104
[26] Guo S, Hu C and Zhang H 2020 Ultra-wide unidirectional infrared absorber based on 1D gyromagnetic photonic crystals concatenated with general Fibonacci quasi-periodic structure in transverse magnetization *J. Opt.* **22** 105101
[27] Yu X, Ohta M, Takizawa N, Mikame K, Ono S and Bae J 2019 Femtosecond-laser-fabricated periodic tapered structures on a silicon substrate for terahertz antireflection *Appl. Opt., AO* **58** 9595–602
[28] Palik E D 1998 *Institute for Physical Science and Technology University* (Maryland College Park: Maryland)
[29] Tolmachev V A, Granitsyna L S, Vlasova E N, Volchek B Z, Nashchekin A V, Remenyuk A D and Astrova E V 2002 One-dimensional photonic crystal obtained by vertical anisotropic etching of silicon *Semiconductors* **36** 932–5
[30] Goto T, Dorofeenko A V, Merzlikin A M, Baryshev A V, Vinogradov A P, Inoue M, Lisyansky A A and Granovsky A B 2008 Optical tamm states in one-dimensional magnetophotonic structures *Phys. Rev. Lett.* **101** 113902
[31] Mehdian H, Mohammadzahery Z and Hasanbeigi A 2015 Optical and magneto-optical properties of plasma-magnetic metamaterials *J. Phys. D: Appl. Phys.* **48** 305101
[32] Qi L, Yang Z, Lan F, Gao X and Shi Z 2010 Properties of obliquely incident electromagnetic wave in one-dimensional magnetized plasma photonic crystals *Phys. Plasmas* **17** 042501
[33] Zhu W, Xiao F, Kang M and Premaratne M 2016 Coherent perfect absorption in an all-dielectric metasurface *Appl. Phys. Lett.* **108** 121901
[34] Maharana P K, Jha R and Padhy P 2015 On the electric field enhancement and performance of SPR gas sensor based on graphene for visible and near infrared *Sensors Actuators B* **207** 117–22
[35] Beheiry M E, Liu V, Fan S and Levi O 2010 Sensitivity enhancement in photonic crystal slab biosensors *Opt. Express, OE* **18** 22702–14
[36] Xuan L, Kong X, Wu J, He Y and Xu Z 2021 A smoothly-connected crescent transverse gradient coil design for 50mT MRI system *Appl. Magn. Reson.* **52** 649–60
[37] Wan B-F, Zhou Z-W, Xu Y and Zhang H-F 2021 A theoretical proposal for a refractive index and angle sensor based on one-dimensional photonic crystals *IEEE Sens. J.* **21** 331–8